Soft Matter

PAPER
J. Wan and H. A. Stone
Microfluidic generation of a high volume fraction of bubbles in droplets

PAPER
A. Javadi *et al.*
Adsorption of alkanes from the vapour phase on water drops measured by drop profile analysis tensiometry.

RSCPublishing

1744-683X(2010)6:19;1-K

Microfluidic generation of a high volume fraction of bubbles in droplets†

Jiandi Wan and Howard A. Stone*

We present a microfluidic approach for the generation of water droplets containing a high volume fraction of gas bubbles and we provide a design principle for microbubble-based pressure sensing inside channels.

Introduction

Micrometre-diameter gas bubbles and particles are the basic elements for making a variety of biomedical materials, such as ultrasound contrast agents,[1,2] drug delivery vehicles[3,4] and materials for the destruction of tumors and thrombus.[5,6] In particular, thin-shell covered microbubbles[7–9] and porous particles[10–12] have been demonstrated for ultrasound imaging and pulmonary drug delivery. Nevertheless, lipid-covered microbubbles produced through sonication[13] or mechanical agitation suffer from a broad size distribution. In addition, hollow or porous particles fabricated using a template-based core–shell approach[9] or pore-forming agents[14] suffer from the use of harmful template-removing chemicals. Not surprisingly, for these applications, the size distribution and stability of the bubbles and the excipients in the formulation of porous particles are continually being investigated and improved.

Microfluidic approaches have been used to generate mono-disperse lipid-encapsulated microbubbles[15,16] and solid polymer particles.[17–19] We previously reported a microfluidic method where porous microparticles can be made by polymerizing monomer-containing water droplets that encapsulate a controlled number of microbubbles.[20] The size of the pores of the obtained particles is determined by the diameter of the encapsulated bubbles, which is at the scale of tens of micrometres in our experimental setup. Although other methods, *e.g.*, template-based core–shell approaches, are able to achieve much smaller pore sizes (*e.g.*, 10–100 nm), our approach shows the advantages of making monodisperse porous particles based on "empty" templates, *i.e.*, bubbles, and there is no need to remove templates after the synthesis. Most importantly, this method is also capable of fabricating thin-shell covered microbubbles and highly porous microparticles so long as a high volume fraction of gas bubbles can be achieved inside the water droplets.

Herein, we report the observation of micrometre-diameter droplets encapsulated with a high volume fraction of gas bubbles, which are formed from the breakup of parent gas-filled droplets at the downstream corners of a rectangular microfluidic channel. This approach takes advantage of the capillary instability of the encapsulating liquid droplets. In addition, we observe that the size of the encapsulated bubbles changes along the microfluidic channel, which we explain as due to the pressure change inside the channel. We also provide an analytical description to quantify the relation between the change of bubble size (δ) and position (z) along the channel. The pressure (relative to a reference) at specific positions in the microfluidic channel can then be determined. The ideas reported here offer new approaches to manipulate gas-in-water-in-oil multiphase flows to obtain droplets with high gas fractions. In addition, we also provide a constructive strategy to monitor pressures inside channels using microbubbles.

Experimental

Microfluidic chips were fabricated in PDMS using standard soft photolithography techniques. The water and oil were loaded in two syringes (Hamilton) respectively and connected to syringe pumps (Kd Scientific, KDS101). Pressure was applied to the needle independently controlled by a regulator (Bellofram, St Louis, MO) with a precision of 0.1 psi. Polyethylene (PE 20) tubes were connected from the syringe needle to the inlet hole of the channel of the device. Before use, the microfluidic chips were treated with octadecyltrichlorosilane (OTS) to make the glass surface hydrophobic.

The illustrations of the microfluidic devices are shown in Fig. 1A. The height of the channels is everywhere equal to 38 μm as measured with surface profilometer. The widths of the gas and water channels are 100 μm; the width of the central channel where gas bubbles were dispersed in the water phase is 60 μm; the width of the oil channel is 200 μm; and the width of the orifice is 20 μm. For the flow-rate dependent measurements, we dispersed pure nitrogen gas bubbles into deionized water with sodium dodecyl sulfate (SDS) (2 wt%, Aldrich) after which the water droplets with bubbles were dispersed into the PDMS 200 oil (viscosity 10 cSt, Aldrich). Typical flow speeds were $\langle u \rangle \approx 5\,\mathrm{cm\,s^{-1}}$, which then correspond to Reynolds numbers $\mathrm{Re} = \rho \langle u \rangle h / \mu \approx 0.2$, where ρ ($\sim$0.96 g ml^{-1}) and μ ($\sim$0.02 Pa s^{-1}) are the density and viscosity of the PDMS oil respectively, and h ($= 38\,\mu\mathrm{m}$) is the height of the channel.

Microbubble emulsions are directly observed using a high-speed video camera (Phantom V 9, 1400 frames per second) mounted on the microscope. The areas of the bubbles and droplets are analyzed using a customized image analysis program in Matlab.

Department of Mechanical and Aerospace Engineering, Princeton University, Princeton, NJ, 08544, USA. E-mail: hastone@princeton.edu
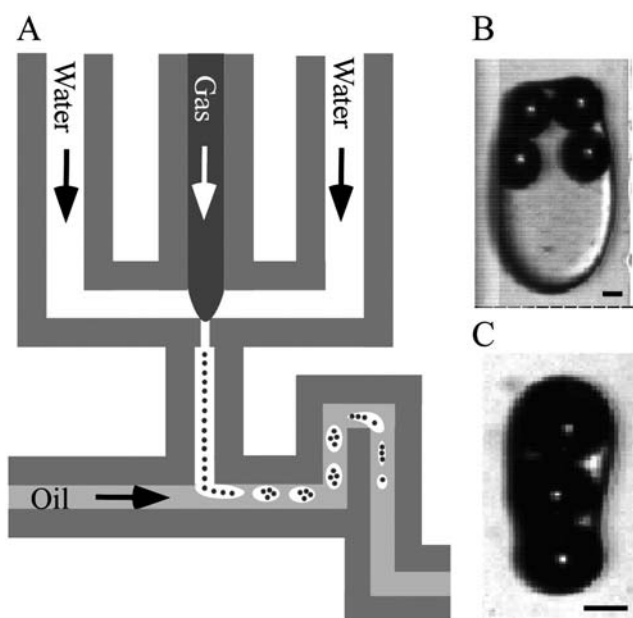
Fig. 1 (A) Schematic of the microfluidic approach for generation of gas-in-water-in-oil emulsions (not to scale). The typical size of the channel is 200 μm (w) × 38 μm (h), except the orifice where the width is 20 μm. (B) Image of a parent water droplet before the breakup process. (C) Image of a secondary water droplet with three encapsulated gas bubbles after the breakup process. Scale bar: 30 μm.

Results and discussion

Water droplets with high volume fraction of gas bubbles

A schematic illustrating the generation of parent water droplets encapsulated with multiple bubbles using a flow-focusing device followed by a T-junction microfluidic channel is shown in Fig. 1A. The typical size of the channel is 200 μm (w) × 38 μm (h), except the orifice where the width is 20 μm. The details of the generation of bubbles encapsulated in water droplets are described in our previous publication;[20] see also the Experimental section above. Briefly, monodisperse microbubbles were first generated in a continuous water phase using a flow-focusing geometry, after which the gas–water system was dispersed into a continuous oil phase by a T-junction element so as to obtain water drops that contain individual gas bubbles. The original water droplets contain a small number of gas bubbles and have a typical gas volume fraction of 0.4 (Fig. 1B). These droplets flow in a continuous oil phase and dynamic effects along the channel, in particular at downstream corners, cause breakup and so generate secondary droplets with fewer bubbles but a higher gas volume fraction (Fig. 1C).

Results for the secondary droplets with different numbers of encapsulated gas bubbles are summarized in Fig. 2A. Secondary droplets with more than one encapsulated bubble have a cylindrical shape after they were generated. Driven by a reduction of surface energy (Fig. S1†), however, the droplets evolve to more compact shapes within milliseconds; *e.g.* contrast the images of the two distinct shapes for each of $N = 3$, 4 and 5 in Fig. 2A. Further, we estimate that the gas volume fraction of the secondary droplets at their compact shapes varies from 0.55 ± 0.08
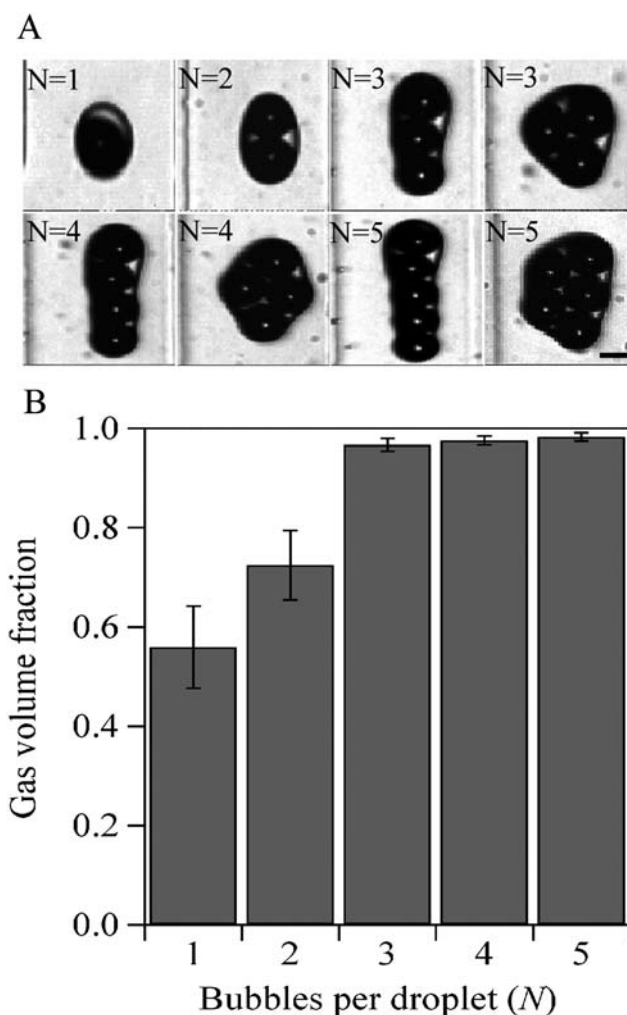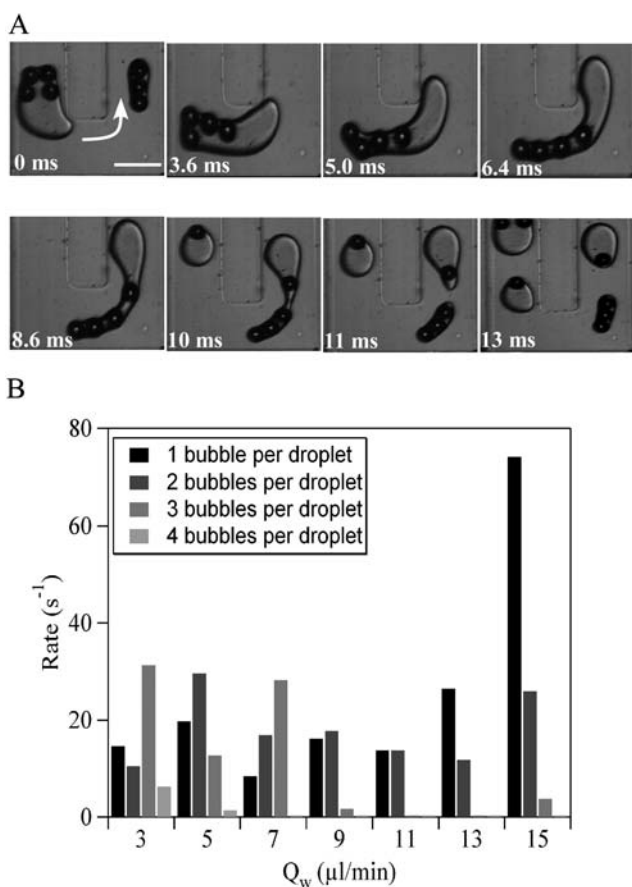

Fig. 2 (A) Images of secondary water droplets with different numbers of encapsulated gas bubbles. For each of $N = 3$, 4 and 5, we show two images, the first is the droplets immediately after breakup and the second more compact shape is obtained following a rapid relaxation driven by surface tension. Scale bar: 50 μm. (B) The gas volume fractions of secondary droplets with different numbers of encapsulated bubbles. For $N = 3$, 4 and 5, the gas volume fraction is calculated based on the compact shape of droplets.

to 0.96 ± 0.005 depending on the number of encapsulated bubbles (Fig. 2B, Fig. S2 and S3†).

Generation and control of the high gas volume fraction water droplets

To understand how the secondary droplets are generated, we examined the dynamics of the parent droplets when they pass around a downstream corner in a channel. Time-lapse images of a breakup process are shown in Fig. 3A. We observe that the parent droplet deforms when it enters the corner section; meanwhile, the encapsulated gas bubbles align as a cylindrical shape inside the rear part of the droplet. The formation of the cylindrical shape inside the parent droplet is presumably due to the deformation of the parent droplet, as a consequence of the higher extension rates in the neighborhood of the corner, which

Fig. 3 (A) Time-lapse images show the generation of a secondary water droplet with three encapsulated gas bubbles. White arrow indicates the flow direction. Scale bar: 200 μm. (B) The effect of water flow rate on the generation of secondary droplets with different numbers of gas bubbles.

will tend to stretch the droplet and so align the bubbles. When the parent droplet passes around the corner, a secondary droplet with a finite number of gas bubbles detaches and forms a high gas volume fraction droplet. Although the details how the secondary water droplets are generated are complicated since it involves surface tension, viscous effects and the geometry of the channel, it is a form of a Rayleigh–Plateau capillary instability. We believe this breakup process is worthy of future investigation.

Based on the qualitative understanding of the generation process of the secondary droplets, we investigate experimental parameters that may impact the process. It is known that the radius of cylinder thread and wavelength play important roles in the Rayleigh–Plateau instability. In our experiment, because it is the bubbles that align along the rear part of the parent droplet forming the cylinder shape thread, the radius of the bubble will be approximately the radius of the cylindrical thread. Therefore, we examine how the bubble radius will affect the generation of secondary droplets by changing the water flow rate: we observe that the higher the water flow rate, the smaller the bubbles, given that the gas pressure and oil flow rate are constant. Fig. 3B shows the experimental results of the effects of applied water flow rate (Q_w) on the generation rate of secondary droplets with different gas bubbles. The results indicate that more secondary droplets are generated with three or four gas bubbles at low water flow

rate than at high water flow rate. Since the size of encapsulated bubbles is larger at low water flow rate, the Rayleigh–Plateau instability will occur at longer wavelength and consequently produce secondary droplets with a higher volume fraction of gas bubbles. In this way, we have identified conditions for obtaining high gas fractions per daughter drop.

Gas bubbles as pressure sensor in microfluidic channel

In addition to the generation of secondary droplets with high gas volume fractions, we also observed a size change of the encapsulated gas bubbles along the microfluidic channel. As shown in Fig. 4A, regardless of the water flow rate, the size of downstream bubbles is invariably larger than that of the upstream bubbles.
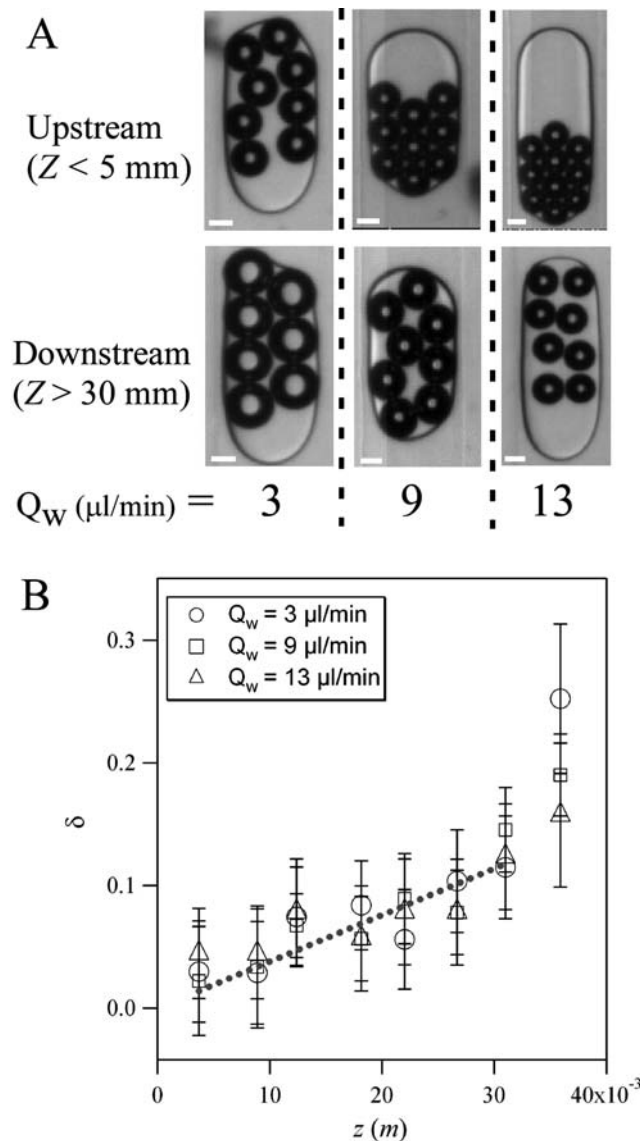
Fig. 4 (A) Images of parent water droplets with encapsulated bubbles at different positions inside the microfluidic channel. Scale bar: 50 μm. (B) The dependence of the fractional change in radius ($\delta = (R(z) - R(0))/R(0)$) of the encapsulated bubbles at the position (z) of the microfluidic channel. $z = 0$ is defined as the middle-point of the first curved channel. Dotted line is the linear fit to the data for $Q_w = 3$ μl min^{-1} given $\delta \le 0.1$.

Since the liquid pressure decreases along the channel, we thus made an idealized analytical calculation to correlate this size change to positions along the channel (Fig. S4†). For the case of a single small bubble in pressure-driven flow and assuming that there are negligible effects of dissolved gas and a small fractional change in radius of the bubble, we define $\delta = (R(z) - R(0))/R(0)$, where $R(z)$ and $R(0)$ are the bubble radius at positions z and $z = 0$ respectively. Note that $z = 0$ can be defined as any position inside the channel where pressure is specified. For the case $\delta \ll 1$, and spherical bubbles, we obtain:

$$\delta \approx \frac{\mu \langle u \rangle z R(0)}{8\gamma k \left(1 + \dfrac{p(0)R(0)}{2\gamma}\right)} \qquad (1)$$

Here, μ, γ and k are the viscosity of water, the surface tension of gas bubbles and the permeability of the channel flow respectively, $\langle u \rangle$ is the average speed of the flow, and $p(0)$ is the pressure at $z = 0$.

We find these results also apply approximately to the case of a more realistic geometric description accounting for the disk-shape of the gas bubbles, which are encapsulated in larger liquid droplets (ESI†). For this case we find:

$$\delta \approx \frac{\mu \langle u \rangle z R(0)}{\gamma k \left(1 + \dfrac{4R(0)}{h} + \dfrac{2p(0)}{\gamma/R(0)}\right)} \qquad (2)$$

The analytical prediction is a linear relation between the change of bubble size and the position along the channel. Further, by plotting δ versus z, the pressure at a specific position inside the channel, e.g., $p(0)$, can be theoretically calculated from the slope. Fig. 4B shows the dependence of δ on z based on the experimental data, where $z = 0$ is defined as the middle-point of the first curved channel. When δ is less than 0.1, we observe a linear relationship between δ and z and the calculated pressure at $z = 0$ is on the order of 10^4 Pa, which is consistent with other pressure measurements inside microfluidic channels.[21] Thus, we believe there is merit to this approximate nonintrusive method of pressure measurement.

Conclusions

In conclusion, because of the rapid developments in multiphase microfluidics, there may be other approaches developed in the future for formation of high gas-to-liquid fraction compound droplets. The present contribution, however, offers a novel microfluidic approach to manipulate multiphase flows using a breakup process that occurs at corners to obtain high gas fractions encapsulated in liquid drops. Finally we provided a design principle for microbubble-based pressure sensing. Based on this technique, further work will focus on the fabrication of functional biomaterials such as ultrasound contrast agents and drug delivery materials.

Acknowledgements

Notes and references

1 K. Ferrara, R. Pollard and M. Borden, *Annu. Rev. Biomed. Eng.*, 2007, **9**, 415–447.
2 J.-U. Voigt, *Methods*, 2009, **48**, 92–97.
3 L. Landini, M. F. Santarelli, L. Landini and V. Positano, *Curr. Drug Discovery Technol.*, 2008, **5**, 328–332.
4 P. Malyala, D. T. O'Hagan and M. Singh, *Adv. Drug Delivery Rev.*, 2009, **61**, 218–225.
5 V. A. Andrei, *Int. J. Stroke*, 2006, **1**, 26–29.
6 J. Wu and W. L. Nyborg, *Adv. Drug Delivery Rev.*, 2008, **60**, 1103–1116.
7 K. W. Ferrara, M. A. Borden and H. Zhang, *Acc. Chem. Res.*, 2009, **42**, 881–892.
8 C. Chlon, C. Guedon, B. Verhaagen, W. T. Shi, C. S. Hall, J. Lub and M. R. Bohmer, *Biomacromolecules*, 2009, **10**, 1025–1031.
9 P.-L. Lin, R. J. Eckersley and E. A. H. Hall, *Adv. Mater.*, 2009, **21**, 3949–3952.
10 M. M. Arnold, E. M. Gorman, L. J. Schieber, E. J. Munson and C. Berkland, *J. Controlled Release*, 2007, **121**, 100–109.
11 D. A. Edwards, A. Ben-Jebria and R. Langer, *J. Appl. Physiol.*, 1998, **85**, 379–385.
12 K. Koushik, D. S. Dhanda, N. P. S. Cheruvu and U. B. Kompella, *Pharm. Res.*, 2004, **21**, 1119–1126.
13 W. Wang, C. C. Moser and M. A. Wheatley, *J. Phys. Chem.*, 1996, **100**, 13815–13821.
14 L. M. Nolan, L. Tajber, B. F. McDonald, A. S. Barham, O. I. Corrigan and A. M. Healy, *Eur. J. Pharm. Sci.*, 2009, **37**, 593–602.
15 K. Hettiarachchi, E. Talu, M. L. Longo, P. A. Dayton and A. P. Lee, *Lab Chip*, 2007, **7**, 463–468.
16 E. Talu, M. M. Lozano, R. L. Powell, P. A. Dayton and M. L. Longo, *Langmuir*, 2006, **22**, 9487–9490.
17 E. Rondeau and J. J. Cooper-White, *Langmuir*, 2008, **24**, 6937–6945.
18 M. Seo, Z. Nie, S. Xu, M. Mok, P. C. Lewis, R. Graham and E. Kumacheva, *Langmuir*, 2005, **21**, 11614–11622.
19 Q. Xu, M. Hashimoto, T. T. Dang, T. Hoare, D. S. Kohane, G. M. Whitesides, R. Langer and D. G. Anderson, *Small*, 2009, **5**, 1575–1581.
20 J. Wan, A. Bick, M. Sullivan and H. A. Stone, *Adv. Mater.*, 2008, **20**, 3314–3318.
21 N. Srivastava and M. A. Burns, *Lab Chip*, 2007, **7**, 633–637.